Laser acceleration of high-energy protons in variable density plasmas

2009 New J. Phys. 11 023038

(http://iopscience.iop.org/1367-2630/11/2/023038)

New Journal of Physics
The open-access journal for physics

Laser acceleration of high-energy protons in variable density plasmas

P Antici[1,2,3], J Fuchs[1,7], E d'Humières[4,8], J Robiche[1,9], E Brambrink[1], S Atzeni[2], A Schiavi[2], Y Sentoku[5], P Audebert[1] and H Pépin[6]

[1] LULI, Ecole Polytechnique, CNRS, CEA, UPMC, Route de Saclay, 91128 Palaiseau, France
[2] Dipartimento di Energetica, Università di Roma "La Sapienza" and CNISM, Via A. Scarpa 14, 00161 Roma, Italy
[3] Istituto Nazionale di Fisica Nucleare, Via E. Fermi, 40, 00044 Frascati, Italy
[4] Centre de Physique Théorique, Ecole Polytechnique, Route de Saclay, 91128 Palaiseau, France
[5] Physics Department, MS-220, University of Nevada, Reno, NV 89557, USA
[6] INRS-Énergie et Matériaux, 1650 bd. L. Boulet, J3X1S2 Varennes, Que., Canada
E-mail: julien.fuchs@polytechnique.fr

New Journal of Physics **11** (2009) 023038 (12pp)
Received 31 October 2008
Published 20 February 2009
Online at http://www.njp.org/
doi:10.1088/1367-2630/11/2/023038

Abstract. The acceleration of protons, induced by electrons generated by a short-pulse laser, is experimentally investigated when varying the density of the plasma target the laser is interacting with. The experimental results are compared with particle-in-cell (PIC) simulations for which the target conditions are inferred from hydrodynamic simulations. High-energy protons are observed only for the two extreme configurations, namely solid-density foils and near-critical-density plasmas having large gradients. Cold solid foils, however, yield the highest energy protons and best proton beam profiles. As suggested by simulations, near-critical-density plasmas could be optimized to further increase the proton energy.

[7] Author to whom any correspondence should be addressed.
[8] Present address: Centre des Lasers Intenses et Applications (CELIA), UMR 5107 de l'Université Bordeaux I-CNRS-CEA, 351 Cours de la Libération, F-33405 Talence, France.
[9] Present address: CEA IRAMIS, Service des Photons Atomes et Molécules, F9191 Gif sur Yvette, France.

Contents

1. Introduction

Since the first observations of laser-accelerated high-brightness proton beams [1, 2], using ultraintense ($>10^{18}$ W cm^{-2}) short-pulse lasers (30 fs–10 ps) [3], much effort has been put into optimizing the proton source in view of the various applications of these beams [4].

The high current, collimated multi-MeV beams of protons, and of other ions [5] are electrostatically accelerated by hot electrons generated by the ultra-intense laser pulses [6]–[9]. This is the so-called target sheath normal acceleration (TNSA) regime. By using standard laser conditions, the highest energy ions originate from contaminants on the rear surface (i.e. non-laser irradiated) foil surface [7, 10] where there is a sharp target–vacuum interface.

In order to pursue the optimization of the production of the proton beams, various accelerating plasma mediums were tested: cold solid foils [2], [5]–[7], [11, 12], high-density exploded foils [13]–[16] or low-density gas jets [17].

Compared to cold foils, dense exploded foils led to a reduction of the proton maximum energy and to an increase in the beam divergence [15, 16, 18, 19]. This is due to the increased Debye length in the plasma gradients of such foils, which reduces the strength of the accelerating electrostatic field at the target boundaries. The longer the gradient, the lower the proton energy [13, 16, 18]. It thus appeared that using targets with plasma gradients could only degrade the proton acceleration.

However, in the extreme case of a low-density (i.e. $0.1n_c$, where n_c is the plasma critical density $n_c = 1.1 \times 10^{21}/\lambda(\mu\text{m})^2\,\text{cm}^{-3}$) plasma, a forward collimated high-energy ion beam could be observed at high laser intensity [17]. As for cold solid foils, the beam is produced by electrostatic acceleration at the target–vacuum boundary. In [17], a gas jet was used to produce the low-density plasma. Compared to using solid foils, using a gas jet is potentially very attractive as it produces no debris and can be used at a high repetition rate and the density of the plasma can be changed easily under controlled conditions.

It therefore seemed that low-density plasmas could represent an interesting alternative to using cold solid foils to obtain a high-energy, collimated, proton beam. Since the various above-mentioned results were obtained in different conditions, this motivated the present work to evaluate, in the same experiment, the respective merit (i.e. beam spatial and energy distribution) of proton acceleration using high-density solid foils or low-density plasmas.

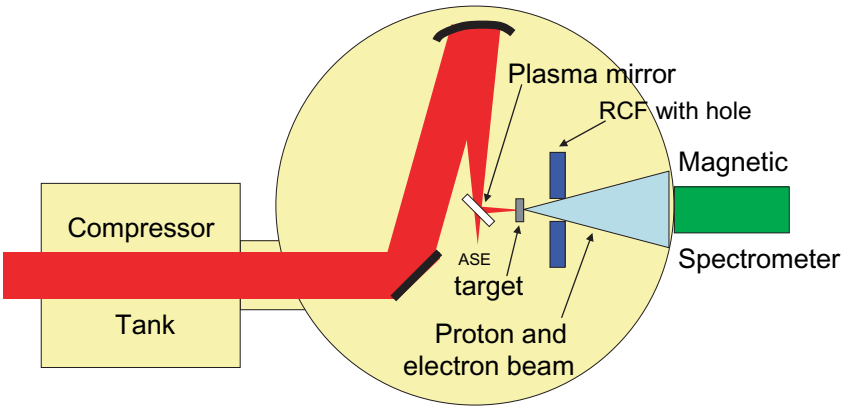

Figure 1. Experimental set-up.

Such a study is performed by quasi-continuously varying the plasma density profile of the proton accelerating medium, as presented in section 2. This variation explores from cold solid foils (i.e. having their rear surface unperturbed) to low-density, long plasmas, as shown in section 3. Section 4 shows that high-energy protons are observed in the two extreme cases (cold solid foils and near-critical-density, long plasmas), although the proton beam profile is noticeably better when using cold solid foils. In section 5.1, the experimental results are compared with particle-in-cell (PIC) simulations for which the target conditions are inferred using hydrodynamic simulations. Cold solid foils exhibit the best proton beam profile and the highest energy protons as the acceleration process at the foil rear surface is not hampered by density gradients and as the laser absorption is highest. The high-energy protons observed for underdense plasmas correspond, according to simulations, to a specific optimum between reduced laser absorption and local electron heating at the target rear surface. Since in this case the shape of the plasma gradient at the target interface is crucial, this latter parameter could be optimized to yield higher energy protons. This is shown in section 5.2 using simulations. Section 6 concludes the study.

2. Experimental set-up

The experiments were performed using the 100 TW laser at the Laboratoire pour l'Utilisation des Lasers Intenses (LULI). The setup of the experiment is shown in figure 1. The wavelength (λ_0) of the laser light is 1.057 μm. The pulse duration is $\tau = 320$ fs, as measured after compression and before focusing. Focusing of the 85 mm diameter beam is achieved using a 300 mm focal length off-axis parabola (i.e. a $f/3.5$ aperture). Wave front correction is applied before every shot to ensure optimum and reproducible focusability [20].

In order to explore various plasma conditions, we have used either Al foils of a few μm thick, or ultrathin silicon nitride (Si_3N_4) planar membranes of 30 nm thickness that were coated with aluminum of variable thickness. We make use of the laser energy contained in the pedestal preleading the main laser pulse to vary the plasma conditions at the time of the main interaction [15, 16, 19]. Thus, varying the thickness of ultrathin targets can produce high-density exploded foils to low density long plasmas. The target thicknesses are 30 nm, 50 nm (30 Si_3N_4 + 20 Al), 100 (30 + 70) nm and 500 (30 + 470) nm. The targets were positioned at the laser focus and were irradiated at normal incidence.

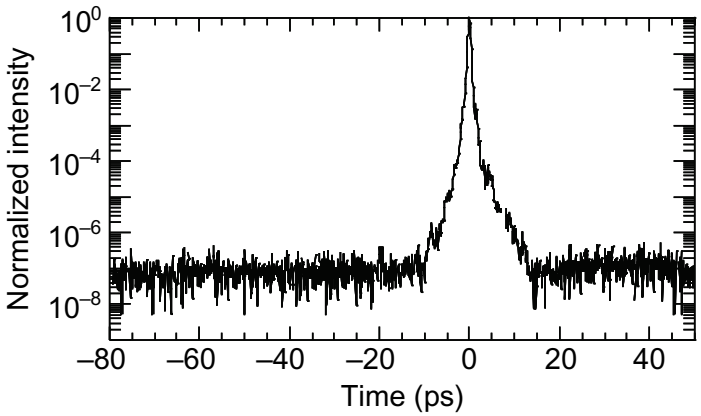

Figure 2. Third-order autocorrelator trace as recorded on the LULI 100 TW laser facility.

In standard conditions, the maximum pedestal (of duration ∼500 ps), resulting from ASE (laser amplified spontaneous emission), is $\sim 4 \times 10^{12}$ W cm^{-2} up to 10 ps before the main pulse, as measured with a high dynamic range third-order autocorrelator [21]. This can be seen in figure 2. However, this pedestal does not allow one to access the desired plasma density profiles as it is of very high intensity. Thus, targets having a thickness of $<0.8\,\mu$m disassembled before the main pulse, so that no proton beam could be detected. Therefore, the pedestal intensity was reduced by setting a plasma mirror (PM [22, 23]) at an intermediate field before focus.

The plasma mirror consists of an anti-reflection-coated optically polished glass slab, so that most of the pedestal energy is transmitted. As the intensity increases in time towards the peak of the pulse, ionization occurs on the plasma mirror interface (through nonlinear mechanisms such as multiphoton absorption). When the electron density in the surface plasma exceeds the critical density n_c at the laser wavelength, the reflectivity suddenly increases and most of the main laser pulse is reflected.

In our experiment, the plasma mirror was positioned so that the fluence on the mirror surface was 44 J cm^{-2}. We measured 0.3% reflection on the PMs at low power, leading to an estimated enhancement of the laser pulse contrast ratio of ∼333 in intensity prior to the main pulse, i.e. a reduced pedestal intensity of $\sim 5 \times 10^{10}$ W cm^{-2} up to 10 ps before the peak of the pulse. To measure the on-target intensity at full power in the main pulse after the plasma mirror, an imaging system was set on the beam path (this was done before installing the proton beam diagnostics shown in figure 1). This system used a collecting lens with a larger aperture ($f/3$) than that of the beam ($f/3.5$). The collected light was sent to both a calorimeter and to an imaging system using a 4× microscope objective coupled to a CCD device. To be able to perform the measurements at full power, a 0°, 99.9% reflectivity mirror was positioned in front of the collecting lens. This ensured that less than 10 mJ went through the lens, so that no nonlinear spurious effects occurred in the imaging optics. With this system, the focal spot after reflection on the plasma mirror was measured to have a full-width at half-maximum (FWHM) of 6 μm. The peak intensity in the spot was $\sim 10^{19}$ W cm^{-2}.

As shown in figure 1, measurement of the proton beam spectrum accelerated from the targets has been performed using a combination of films, which yield a coarse resolution in energy and monitor the beam in the transverse plane, 3 cm away from the target, and a magnetic

spectrometer [24]. The films are radiochromic film (RCF) dosimetry media [25]. RCFs are preferentially sensitive to penetrating protons, which have a large specific energy loss and produce a high contrast image. Electrons and x-rays generally appear as a diffuse low-intensity, low-contrast background that extends over the whole film surface. The absolute calibration between the optical density of the film and the proton deposited energy[10] allows one to retrieve, for each film (corresponding to an energy bin), the number of incident protons. When using the films in parallel with the magnetic spectrometer, located 70 cm away from the target, a central, millimeter-sized hole was bored through the RCF to allow a clear aperture to the spectrometer.

3. Hydrodynamic simulations of interaction conditions

To assess the plasma density profile at the time of the main laser pulse, i.e. the profile resulting from the interaction between the target and the laser pedestal reduced by the PM, we performed hydrodynamic simulations. The hydrodynamics codes were the one-dimensional (1D) code Esther [26] and the two-dimensional (2D) code DUED [27].

Esther solves, according to a Lagrangian scheme, the fluid equation for the conservation of mass, momentum and energy. The target material is described by a multiphase equation of state spanning a large range of density and temperature from hot plasma to cold condensed matter. The interaction between the laser field and the target is given by the solution of the Helmholtz wave equation. This requires accurate values for the conductivity; we used the values from Eberling [28], Palik [29] in the solid phase and the Spitzer formula in the plasma phase. The simulations used 50 cells and 100 time steps.

DUED is also a Lagrangian code and considers a two-temperature (ions and electrons) single fluid. It includes collisional transport coefficients, radiation losses and the equation of state described in [30]. Laser–plasma interaction is dealt with a geometric optics approximation. Absorption by inverse-bremsstrahlung and plasma refraction is taken into account. We simulated the pedestal with a laser beam of constant intensity after an initial linear rise time of 100 ps with FWHM $\sim 6\,\mu$m. The Lagrangian mesh had 60 cells in the initial longitudinal direction with variable cell mass and 30 in the radial dimension.

For both codes, a multilayer target composed of 30 nm of SiO_2 and of a variable thickness of Al (the Al layer being on the laser irradiation side, as in the experiment) was irradiated by the experimentally measured laser pedestal. Results from the two hydrocodes are consistent. In the simulations we used SiO_2 instead of Si_3N_4 since we could not properly simulate Si_3N_4 due to a lack of adequate equation of state. The simulations show that after 500 ps (i.e. the length of the laser ASE), the thickest targets (i.e. thickness $>1\,\mu$m) are essentially unperturbed by the laser pedestal: no detectable plasma gradient is present on the target rear surface. However, for thinner targets, down to 100 nm, a significant rear surface plasma gradient develops, although their peak density stays highly overcritical. For even thinner targets (50 and 30 nm), the peak density decreases significantly, down to under-critical values for the 30 nm target. The electron density profiles at the time of the main laser pulse for these thin targets are illustrated in figure 3.

Note that in these conditions (i.e. for targets <100 nm), the interaction with the ultrathin targets is different from the relativistic transparency regime studied in [31]–[34] for which the targets are still solid at the time of the main pulse.

[10] Deduced from the manufacturer's calibration of the RCFs (http://www.ispcorp.com/) that has been verified by us using a calibrated proton accelerator.

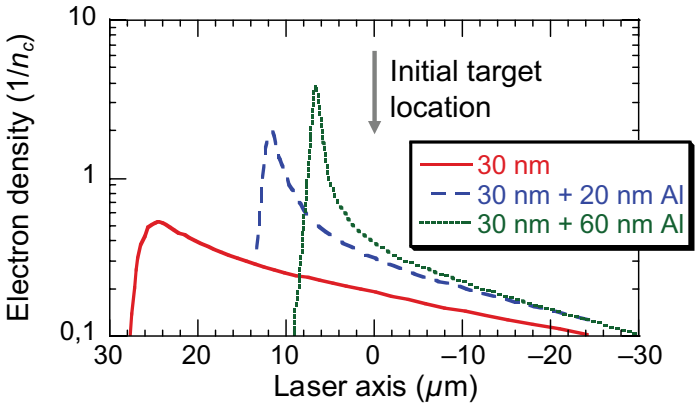

Figure 3. Axial electron density profiles (i.e. at the center of the target) as given by the DUED simulations for a target composed of 30 nm SiO_2 and for two targets with the same layer plus 20 and 60 nm of Al on top (the Al coating being on the laser incident side). The profiles are shown at time $t = 500$ ps after the onset of a laser pedestal with constant intensity $I = 5 \times 10^{10}$ W cm^{-2}. The laser irradiates the target from the right-hand side. The targets are initially located at 0.

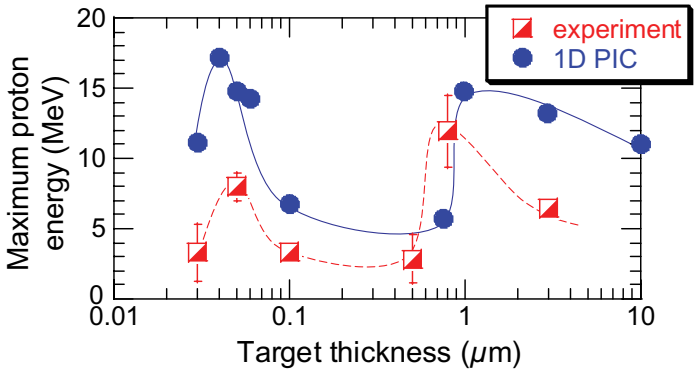

Figure 4. Maximum proton energy versus target thickness using aluminum targets of different thicknesses in intermediate contrast conditions. Dots indicate the 1D PIC simulations, squares the experimental values. Each experimental data point includes several shots (from 2 to 3) and the error bar on energy represents the recorded rms shot-to-shot fluctuation. Error bars for 100 nm and 3 μm are smaller than the box width. Lines are guides for the eye.

4. Experimental results

Figure 4 shows the maximum proton energies recorded by RCFs and the magnetic spectrometer in these various plasma conditions. Each data point includes several shots (from 2 to 3) and the error bar on energy represents the recorded rms shot-to-shot fluctuation. We observe two peaks in the proton energy, one for 1 μm thickness and one for 50 nm, yielding a maximum proton energy of ~8 MeV for the 50 nm target and of ~12 MeV for the 1 μm target. However,

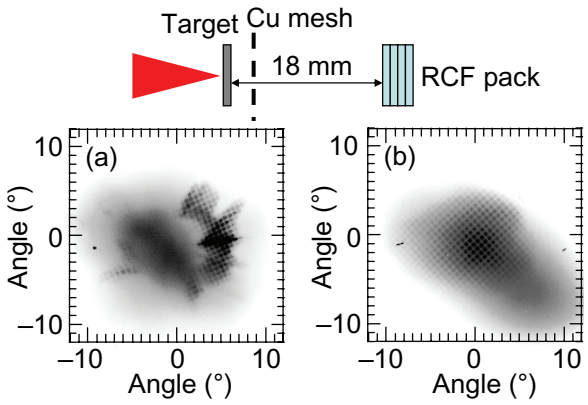

Figure 5. RCF layers corresponding to (a) 8.3 ± 0.3 MeV using a 50 nm-thick target and (b) 9.8 ± 0.2 MeV using a 800 nm-thick target. For these shots, we did not bore a hole in the RCFs to allow a clear aperture for the magnetic spectrometer, so that the complete beam profile could be recorded. As illustrated above the films, a Cu mesh (1000 lines in^{-1}) is placed between the target and the stack of RCF films, 1 mm behind the target. The mesh allows discrimination between protons and electrons within the beam penetrating the RCF stack as the mesh is impressed only on the protons. Although the wires composing the mesh are thin (5 μm), multiple scattering of the laminar [37, 38] protons is enough for the shadows of the wires to be impressed on the proton beam profile [38]. This is not the case for the angularly larger background electron signal superimposed on the proton signal and that is not imprinted by the mesh because electron multiple scattering in the thin wires in very reduced compared to protons. Proton spectra measurements using the downstream magnetic spectrometer (see figure 1) confirm unambiguously that the mesh-imprinted signal corresponds to protons: this signal is seen to stop in a well-defined RCF layer. This layer yields a maximum energy that corresponds to the one of the spectrometer. The non-mesh-imprinted signal continues to be seen much further down the RCF stack, and therefore cannot correspond to protons.

figure 5 shows that the proton beam profiles differ in these two extreme cases. Although relatively collimated, the proton beam from the near-critical-density plasma (the 50 nm foil) is very irregular. On the contrary, the proton beam accelerated from the cold foil (the 800 nm Al foil) is significantly smoother and more circular. Note that the actual absolute maximum of proton energy recorded for near-critical-density plasmas does not necessarily correspond to the 50 nm target since, for technical reasons, we were not able to vary continuously the target thickness around that value. The absolute maximum could therefore correspond to a thickness around 50 nm. Of course, this maximum observed in our experiment depends entirely on the prepulse conditions and would occur at a different target thickness for different experimental conditions. However, by scanning over the various available target thicknesses, it does appear clearly that there is a local maximum in proton energy for very thin targets, this maximum being repeatable here for 50 nm over a series of shots. This is the main result of our study, i.e. to show that efficient proton acceleration can take place in partially decompressed targets, the efficiency of the acceleration being at least close to the one obtained from solid targets.

The results obtained by scanning over the target thickness were partly expected: for thick targets, i.e. thicker than 0.8 μm (for which the target rear surface is not perturbed), the decrease in the maximum proton energy with the target thickness is due to the ballistic spray of the electrons within the increasing target volume [11, 19]. Indeed, this reduces the accelerating potential at the target rear surface. The drop in the proton energy for targets thinner than 1 μm is also expected. Indeed, the hydrodynamic simulations presented in section 3 show that the rear surface of such targets is perturbed by the laser pedestal. This perturbation leads to a gradient on the target rear surface, which then reduces the accelerating electric field strength [18], as discussed in section 1. The results for the thinner targets, especially the unexpected proton energy increase observed for a specific thickness, will now be discussed.

5. Discussion

5.1. Simulations of the present experiment

To support the above interpretation of the results and go beyond, we have performed simulations using the 1D PIC code PICLS [35]. For each target, its density profile as obtained from the hydrodynamic simulations is used as an input in the simulations. For the unperturbed solids, we have used a maximum density of $100n_c$. The incident laser pulse has a 1 μm wavelength, a 350 fs pulse duration and an intensity of 10^{19} W cm^{-2}. The temporal profile is a truncated Gaussian. The target is initially fully ionized, and consists of electrons and protons. The simulation box is 600 μm long. The target front surface is located 200 μm from the left boundary of the simulation box where the laser enters. The mesh size is $\Delta x = 6$ nm and there are 100 protons and electrons per cell. The time step is equal to 2×10^{-2} fs.

As shown in figure 4, the variations of the maximum proton energy around the 1 μm thick target observed in the PIC simulations are well consistent with the experimental results. These variations are due to larger targets in which the electrons spread and thinner targets where rear-surface gradients reduce the accelerating field. Note that for all target thicknesses the simulated proton energy is overestimated. This overestimate is expected in the 1D geometry: as the transverse spreading of the electrons within the target is not accounted for, the electron density at the target rear surface, and thus the accelerating field strength are overestimated.

Regarding the very thin targets exploded to large, low-density plasmas (see figure 3), the PIC simulations also exhibit a local peak in the proton energy. This is shown in figure 4 around the 40 nm thick target. This local peak could result from a specific optimum between opposite tendencies. On the one hand, two effects concur to reduce the proton accelerating field when reducing the target thickness: (i) thinner targets result in larger rear-surface gradients and (ii) interacting with low-density plasmas reduces the laser absorption. The latter point is illustrated in figure 6. On the other hand, we speculate that extended laser propagation within the low-density plasma allows generation of hot electrons directly at the target rear surface. This is based on the fact that we observe, for the near-critical-density targets, the maximum energy protons to be indeed accelerated at the target rear surface. This is evidenced in figure 7 which shows phase-space plots from two simulations, one for the 30 + 20 nm target (50 nm total) (figure 7(a)) and one for the 10 μm target (figure 7(b)) i.e. in the standard well-known TNSA regime. We can observe that in both cases, the maximum energy protons indeed originate from the target–vacuum rear interface. An efficient electron generation at the target rear, after the laser propagation through the target, would increase locally the proton accelerating electric field. This

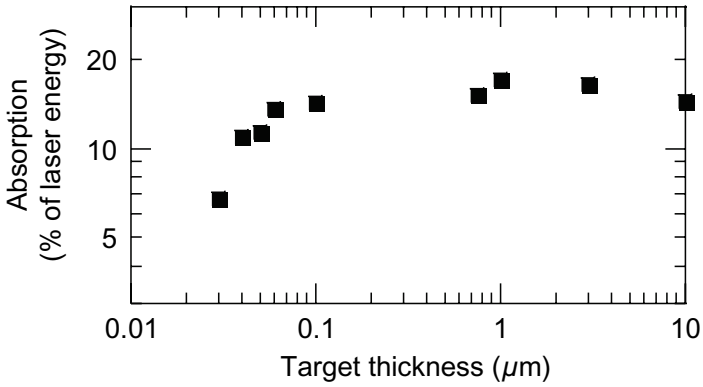

Figure 6. Simulated absorbed fraction of the laser energy (in %) versus target thickness using targets of different thicknesses in intermediate contrast conditions.

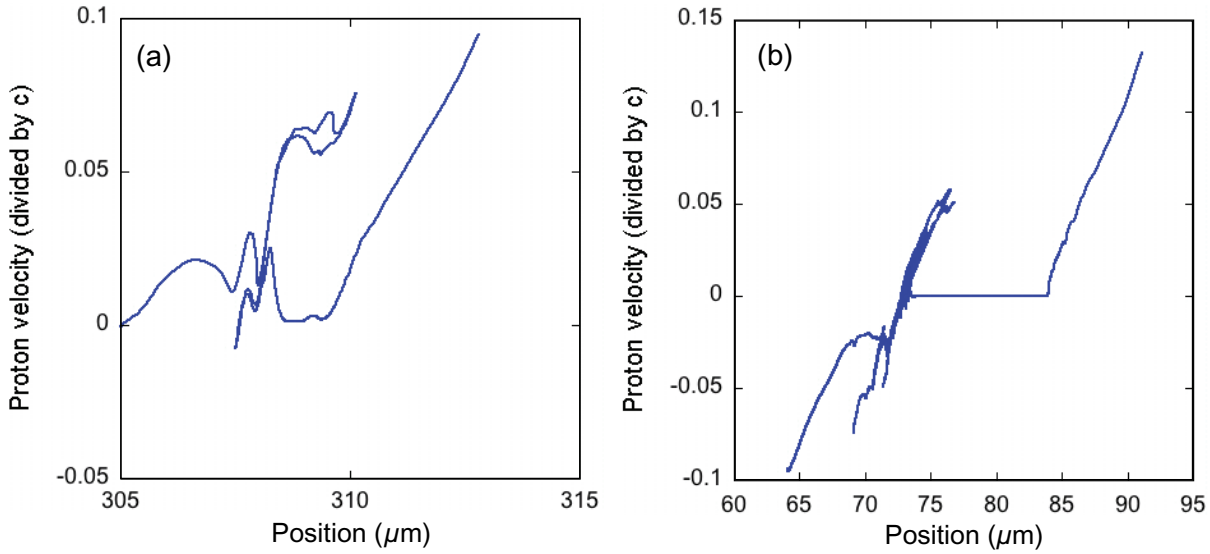

Figure 7. Transverse phase space plots as given by the 1D PIC simulations (a) for a target of 50 nm total thickness and 500 fs after the beginning of the interaction (i.e. the laser irradiating the target) and (b) for a target of 10 μm total thickness and 600 fs after the beginning of the interaction. The laser originates from the left of the figure.

is in comparison with the case of overcritical targets where the electrons can be generated only at the target front surface. The plasma profile resulting from the exploded 40 nm target (where density decreases to below n_c during the main pulse irradiation) would then correspond to such an optimum.

Note that, as the PIC simulations are 1D, although the trend shown in figure 4 is comparable to the one observed in the experiment, one has to bear in mind that other factors, where a higher dimensionality will play a role, are also important to understand the proton energy variations: target geometry for the cases where a plasma is preformed behind the target (i.e. for targets

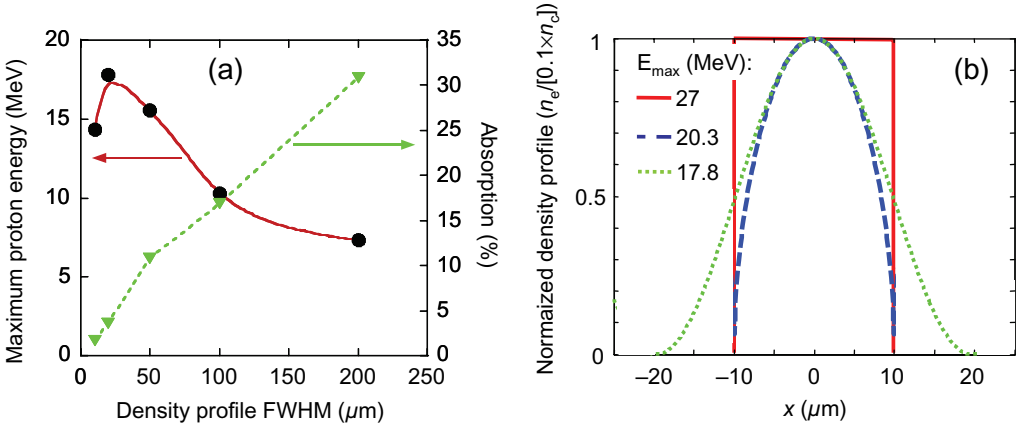

Figure 8. (a) Simulations of (•, left scale) the maximum proton energy accelerated from a low-density plasma having a peak density of $0.1n_c$ but variable FWHM length, as indicated in the abscissa. The plasma profile varies as $\cos^2(x)$, from 0 to the peak density, as the profile shown in dashed in (b). The laser absorption in the same plasma is also indicated (triangles, right scale). (b) Various plasma profiles (all having a peak density of $0.1n_c$) with the maximum proton energy accelerated from each plasma profile as indicated in the plot.

thinner than 750 nm) and laser propagation through the target for the thinner exploded target cases (i.e. for targets thinner than 50 nm).

5.2. Potential optimization of low-density plasmas

The plasmas explored in the experiment are all relatively thin. To see what would be the effect of extending the length of a low-density target, we performed additional simulations. Figure 8(a) shows the simulated maximum proton energy and laser absorption obtained when varying the length of a low-density plasma at a fixed peak density of $0.1n_c$ and for the same laser parameters as used in figure 4. Shorter plasma (for the same peak density) means sharper gradients, but also reduced absorption. As can be seen in figure 8(a), it is rather the sharpness of the gradient, compared to having strong laser absorption, that seems to be crucial to obtain the highest energy protons. This is confirmed by figure 8(b) in which the plasma FWHM length and the peak density are kept constant while the sharpness of the target–vacuum interface is varied. As is manifested by the maximum proton energies obtained in the three explored cases (see values in figure 8(b)), the sharpest low-density plasmas indeed yield the highest proton energies. This was expected as the acceleration mechanism is the same as in the high-density foils for which the sharpness of the gradient at the target–vacuum interface is equally crucial. Further extensive exploration of the optimum conditions (plasma shape and density, and laser conditions) for laser-generated of protons in low-density plasmas, as will be useful to guide future experiments, will be reported in a separate theoretical publication [36].

Note that such optimization of the low-density plasma could be very attractive since the maximum proton energy thus obtained (27 MeV with the parameters here explored, with room for further optimization) is significantly higher than the one obtained using solid foils (12 MeV,

see figure 4), thanks to the local heating of the electrons at the accelerating interface. The practical feasibility of such a sharp low-density plasma is, however, to be demonstrated.

6. Conclusion

In summary, we have shown that there are two favorable plasma conditions for acceleration of high-energy protons: (i) cold solid foils where there is no plasma gradient at the accelerating interface and (ii) near-critical-density plasmas where a compromise between reduced laser absorption and local electron heating at the proton accelerating plasma–vacuum interface results in high accelerating fields. Although in the present experiment, the beam profile produced from the near-critical-density plasma is of poor quality, simulations show that regarding the proton energy, this configuration can be significantly optimized if sharp interface plasmas are used. For a given laser intensity, this would allow one to produce higher energy protons than when using cold solid foils, even if of lower quality.

Acknowledgments

We acknowledge the expert support of the LULI laser team. We also express our gratitude to Patrick Combis from Commissariat à l'Énergie Atomique for his support in the use of the code Esther provided by CEA. This work was supported by grant ANR-06-BLAN-0392 from ANR-France, DAAD, grant no. E1127 from Région Ile-de-France, UNR DoE/NNSA grant no. DE-FC52-01NV1405, and the Italian MIUR project no. FIRB RBNE03N48B 'BLISS'.

References

[1] Clark E L *et al* 2000 *Phys. Rev. Lett.* **84** 670
Krushelnick K *et al* 2000 *Phys. Plasmas* **7** 2055
Maksimchuk A *et al* 2000 *Phys. Rev. Lett.* **84** 4108
[2] Snavely R A *et al* 2000 *Phys. Rev. Lett.* **85** 2945
[3] Strickland D and Mourou G 1985 *Opt. Commun.* **56** 219
[4] Borghesi M *et al* 2006 *Fusion Sci. Technol.* **49** 412
[5] Hegelich B M *et al* 2002 *Phys. Rev. Lett.* **89** 085002
[6] Fuchs J *et al* 2005 *Phys. Rev. Lett.* **94** 045004
[7] Allen M *et al* 2004 *Phys. Rev. Lett.* **93** 265004
[8] Hatchett S *et al* 2000 *Phys. Plasmas* **7** 2076
[9] Mora P 2005 *Phys. Rev.* E **72** 056401
[10] Gitomer S J *et al* 1986 *Phys. Fluids* **29** 2679
[11] Fuchs J *et al* 2006 *Nat. Phys.* **2** 48
[12] Robson L *et al* 2007 *Nat. Phys.* **3** 58
[13] Yogo A *et al* 2008 *Phys. Rev.* E **77** 016401
[14] Matsukado K *et al* 2001 *Phys. Rev. Lett.* **91** 215001
[15] Xu M H *et al* 2006 *Phys. Plasmas* **13** 104507
[16] Wang X *et al* 2005 *Phys. Plasmas* **12** 113101
[17] Willingale L *et al* 2006 *Phys. Rev. Lett.* **96** 245002
[18] Grismayer T and Mora P 2006 *Phys. Plasmas* **13** 032103
Fuchs J *et al* 2007 *Phys. Rev. Lett.* **99** 015002
[19] Kaluza M *et al* 2004 *Phys. Rev. Lett.* **93** 045003

[20] Wattellier B *et al* 2004 *Opt. Lett.* **29** 2494
[21] Salin F 1987 *Appl. Opt.* **26** 21
[22] Monot P 2004 *Opt. Lett.* **29** 893
[23] Lévy A *et al* 2007 *Opt. Lett.* **32** 310
[24] Mančic A *et al* 2008 *Rev. Sci. Instrum.* **79** 073301
[25] Klassen N V *et al* 1997 *Med. Phys.* **24** 1924
[26] Colombier J P *et al* 2006 *Phys. Rev.* B **71** 165406
[27] Atzeni S *et al* 2005 *Comput. Phys. Commun.* **169** 153
Atzeni S 1986 *Comput. Phys. Commun.* **43** 107
[28] Ebeling W, Förster A, Fortov V, Griaznov V and Polishchuk A 1991 *Thermophysical Properties of Hot Dense Material* (Stuttgart: Teubner)
[29] Palik E D 1985 *Handbook of Optical Constant of Solids I* (New York: Academic)
Palik E D 1991 *Handbook of Optical Constant of Solids II* (New York: Academic)
[30] Atzeni S, Caraso A and Pais V A 1986 *Laser Part. Beams* **4** 393
[31] d'Humières E *et al* 2005 *Phys. Plasmas* **12** 062704
Dong Q *et al* 2003 *Phys. Rev.* E **68** 026408
Yin L *et al* 2006 *Laser Part. Beams* **24** 291
[32] Neely D *et al* 2006 *Appl. Phys. Lett.* **89** 021502
[33] Antici P *et al* 2007 *Phys. Plasmas* **14** 030701
[34] Ceccotti T *et al* 2007 *Phys. Rev. Lett.* **99** 185002
[35] Sentoku Y and Kemp A 2008 *J. Comput. Phys.* **227** 6846
[36] d'Humières E to be published
[37] Cowan T E *et al* 2004 *Phys. Rev. Lett.* **92** 204801
[38] Borghesi M *et al* 2004 *Phys. Rev. Lett.* **92** 055003